High-energy electronic excitations in a bulk MoS$_2$ single crystal

Binbin Yue,[1,2] Fang Hong,[1,2,*] Ku-Ding Tsuei,[3] Nozomu Hiraoka,[3] Yu-Han Wu,[3] Vyacheslav M. Silkin,[4,†]
Bin Chen,[1,‡] and Ho-kwang Mao[1,5]

[1]*Center for High Pressure Science and Technology Advanced Research, 1690 Cailun Road, Pudong, Shanghai 201203, China*
[2]*Advanced Light Source, Lawrence Berkeley National Laboratory, Berkeley, California 94720, USA*
[3]*National Synchrotron Radiation Research Center, Hsinchu, 30076, Taiwan*
[4]*Donostia International Physics Center (DIPC), Paseo de Manuel Lardizabal 4, 20018 San Sebastián/Donostia, Spain;*
Departamento de Física de Materiales, Universidad del País Vasco, Apartado 1072, 20080 San Sebastián/Donostia, Spain;
and IKERBASQUE, Basque Foundation for Science, 48011 Bilbao, Spain
[5]*Geophysical Laboratory, Carnegie Institution of Washington, Washington, DC 20015, USA*

The collective electronic excitations and their dispersion behavior across both the first and second Brillouin zones in a bulk MoS$_2$ single crystal have been investigated using nonresonant inelastic hard x-ray scattering and time-dependent density-functional theory. The experiment results revealed two main plasmons located around 8.6 and 23 eV. The ~8.6 eV plasmon shows clear anisotropic behavior and was only observed in plane due to the two-dimensional geometry. In addition, theoretical calculation indicates that the dispersion behavior of this in-plane plasmon shows weak momentum dependence. The main plasmon near 23 eV demonstrates an isotropic three-dimensional collective electron excitation behavior, which suggests a weak correlation between the electron excitation and layered lattice structure. This behavior is completely different from the anisotropic dispersion behavior found in layered graphite. Our work provides clear experimental and theoretical data on the dynamic electronic behavior of excited high-energy electrons in MoS$_2$, which not only provides guidance on device design but also furthers understanding of electronic behaviors in other similar systems.

I. INTRODUCTION

Two-dimensional (2D) materials have been widely studied for their unique structural, physical, and chemical properties [1–3]. Graphene is a type of 2D material with a hexagonal structure; it shows great potential for industrial electronic device and energy material applications [4–7]. Hexagonal boron nitride (*h*-BN) is an analog insulator for semimetallic graphite and is expected to be an ultraviolet laser material with excellent performance [8–10]. Transition-metal dichalcogenides (TMDs) have a similar layered hexagonal structure and attract great interest due to their excellent mechanical and electronic properties [11–14]. The chemical formula of the TMD is MX_2, where M is a transition metal and X is a chalcogen (S, Se, and Te). In general, they are built up from hexagonally packed layers consisting of a transition-metal atom plane sandwiched between two planes of chalcogen atoms in a trigonal prismatic arrangement. The properties of these materials are very anisotropic like graphite, with their covalent bonding in one layer (σ bond) and weak van der Waals bonding between layers (π bond). TMD materials display metallic or semiconducting/insulating behavior depending on the transition metal (M). NbSe$_2$ is a metallic system which exhibits remarkable low-temperature phenomena, including the competition between superconductivity and the charge-density wave order [15,16]. WS$_2$ and MoSe$_2$ are both semiconducting materials with an indirect band gap in their bulk form [17,18].

Recently, many groups have focused their efforts on 2D structured MoS$_2$. Bulk MoS$_2$ is an indirect optical band-gap semiconductor (1.2 eV), while single-layer MoS$_2$ displays a direct optical band gap of about 1.8 eV, as proven by some theoretical and experimental works [19,20]. It bridges the gap between gapless graphite/graphene and *h*-BN with a large band gap, and is a promising material for optoelectronic applications [13,21]. Field-effect transistors have been made successfully based on MoS$_2$ [22,23]; Wu *et al.* reported weak piezo-electric behavior in single-layer MoS$_2$ [14] which provides the possibility of designing multifunctional optoelectronic devices using this kind of 2D material. To help design future optoelectronic devices, it is necessary to understand their electronic properties in an excited state and their dielectric screening effect. Studying the collective electronic excitation provides an essential insight into the electronic structure of MoS$_2$ and other similar TMD materials (which are important for both industrial applications and fundamental research) and reveals their dynamic electronic behavior (such as dielectric response and screening effect) which is directly related to device applications [24,25]. Inelastic x-ray scattering (IXS) is a primary and highly efficient technique to complete this work. Unlike electron energy-loss spectroscopy (EELS) experiments carried out with a transmission electron microscope, inelastic hard x-ray scattering is particularly suitable for experiments with large momentum transfer out of the first Brillouin zone [26]. Therefore, it is possible to probe the plasmon dispersion and look at the effects of the short-range part of its Coulomb interaction. Previously, Cudazzo *et al.* have measured the high-energy collective electronic excitation in metallic TMDs by IXS. However, only limited spectra at limited Q points along the *c* axis have been collected [27]. In this work, we conducted both IXS experiments and *ab initio* calculations to investigate

---

*fhong@lbl.gov
†vyacheslav.silkin@ehu.eus
‡chenbin@hpstar.ac.cn

MoS$_2$ single-crystal high-energy collective excitations and their dispersion behavior on all high-symmetry directions.

II. EXPERIMENTAL DETAILS

The IXS experiment was performed at the Taiwan inelastic x-ray scattering beamline BL12XU at SPring-8, which was designed for studies on various types of electronic excitations. The synchrotron radiation from an undulator was monochromated by a Si (111) double-crystal monochromator. The energy resolution was ~2 eV, as determined by the bandwidth of the quasielastic peak. The beam was focused to a 120×80-μm^2 spot on the sample by a Pt-coated Si focusing mirror. The signal was collected with a Si (777) analyzer and finally detected by a Si diode. The bending radius of the analyzer was 2 m and the momentum resolution was about 0.25 Å^{-1}. The analyzer Bragg angle was fixed at 87.6° and the spectra were recorded from $+2$ to $+50$ eV for the inelastic peaks and -5 to $+5$ eV for the elastic peaks around a nominal incident energy of 13843 eV (E_0). One spectrum took about 2–3 h for a single momentum transfer. The measurements were carried out at room temperature.

III. *AB INITIO* CALCULATIONS

According to the fluctuation-dissipation theorem [28] the rate of momentum ($\bm{Q}$) and energy (ω) transfer to the system from a probe is determined by the dynamical structure factor $S(\bm{Q},\omega)$ relationship between a periodic crystal and the dynamical dielectric function matrix $\varepsilon_{\bm{GG'}}(q,\omega)$ as

$$S(\bm{Q}, \omega) = -\frac{\Omega|\bm{G}+q|^2}{2\pi}\text{Im}\big[\varepsilon_{GG}^{-1}(\mathbf{q},\omega)\big], \quad (1)$$

where $\bm{G}$ is the reciprocal lattice vector, $\bm{Q} = \bm{G} + \bm{q}$ with vector $\bm{q}$ being in the first Brillouin zone, and Ω is the normalization volume. The inverse dielectric function is related to the density-response function of interacting electrons χ through $\varepsilon^{-1} = 1 + \upsilon\chi$, where υ is the Coulomb potential. In the framework of the time-dependent density-functional theory [29,30] χ obeys the integral equation $\chi = \chi + \chi^\circ(\upsilon + K^{xc})\chi$, where χ° is the response function for a noninteracting electron system and K^{xc} accounts for dynamic exchange-correlation effects.

The imaginary part of the χ° function was calculated, using our homemade code [31], according to

$$\chi_{GG'}^{oI}(\mathbf{q},\omega) = \frac{2}{\Omega}\sum_{\mathbf{k}}^{\text{BZ}}\sum_{n}^{\text{occ}}\sum_{n'}^{\text{unocc}}\delta(E_{n\mathbf{k}} - E_{n'\mathbf{k}+\mathbf{q}} + \omega)\langle\psi_{n\mathbf{k}}|$$
$$\times e^{-i(\bm{G}+\mathbf{q})\mathbf{r}}|\psi_{n'\mathbf{k}+\mathbf{q}}\rangle\langle\psi_{n'\mathbf{k}+\mathbf{q}}|e^{i(\bm{G'}+\mathbf{q})\mathbf{r}}|\psi_{n\mathbf{k}}\rangle, \quad (2)$$

where the factor of 2 accounts for spin, n and n' are the band indices, $\bm{k}$ is in the first Brillouin zone (BZ), and $E_{n\mathbf{k}}$ and $\psi_{n\mathbf{k}}$ are Bloch eigenvalues and eigenfunctions of the Kohn-Sham Hamiltonian. Subsequently, the real part of χ° was calculated using the Kramers-Kronig relation.

We obtained the single-particle energies and wave functions from the self-consistent solution of the Kohn-Sham equations using the pseudo-potential band-structure code [32]. In this calculation the local exchange-correlation potential was employed in the form of Ref. [33]. The electron-ion
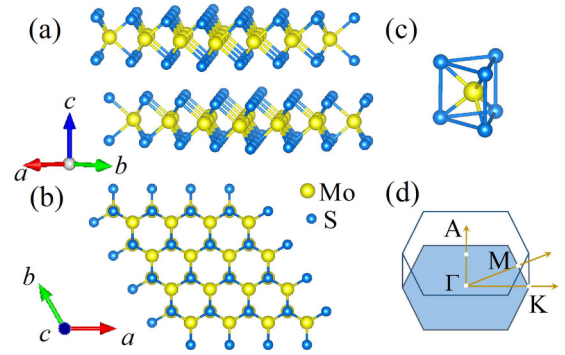
interaction was described by a nonlocal norm-conserving ionic pseudopotential [34]. Up to 100 reciprocal lattice vectors ($\bm{G}$) were included in the Fourier expansion of χ°,χ, and ε matrices. In Eq. (2) we used a $60 \times 60 \times 24$ mesh for the $\bm{k}$ summation and the sum over n and n' included 150 bands. For the description of K^{xc}, two forms were employed: a random-phase approximation (RPA) (i.e., $K^{xc} = 0$) and the time-dependent local density approximation (TD-LDA) of Ref. [35].

IV. RESULTS AND DISCUSSIONS

A. IXS energy-loss spectra of MoS$_2$

The MoS$_2$ single-crystal sample we used in our experiment was exfoliated mechanically from a bulk crystal to about 70 μm thick to reach a maximum scattering efficiency. Its layered structure scheme is presented in Figs. 1(a)–1(c). The atomic structure of MoS$_2$ is very similar to graphite; both Mo and S layers form a honeycomb structure. However, monolayer MoS$_2$ consists of three atomic layers, rather than the single atomic layer in graphite, which makes its unit cell much larger than graphite. We collected IXS spectra along the ΓM, ΓK, and ΓA symmetry directions (reciprocal space), respectively, as shown in Fig. 1(d). To align the direction of the single crystal, we collected diffraction patterns for the ΓM and ΓK directions (see the Supplemental Material [36]).

The collected spectra were normalized with an incident intensity monitor signal and the constant background was subtracted from the result. The inelastic x-ray scattering spectra (IXS) at various momentums ($\bm{Q}$) are plotted in Fig. 2. The IXS spectra were fitted using the Voigt function with a Gaussian component of about 2 eV full width at half maximum (FWHM) corresponding to the experimental energy resolution (the value for each spectrum was obtained from fitting the relevant quasielastic peak). One fitting example is shown in Fig. S2 and the relevant parameters can be found in Table S1 [36]. The raw spectra are plotted in the form of scattered dots while the fitted spectra are plotted with a solid line.

For $\bm{Q}//\Gamma K$, eight spectra presented in Fig. 2(a) were obtained from $\bm{Q} = 0.184$ Å^{-1} (which is the closest to the Γ point) to $\bm{Q} = 2.65$ Å^{-1}, the 2 K point in the Brillouin zone.

FIG. 1. The structure of MoS$_2$ crystal in real and reciprocal space. (a) Side view and (b) top view of the bulk MoS$_2$ atomic/lattice structure along the c axis; (c) the simplest unit of MoS$_2$ molecular; (d) the first Brillouin zone of the MoS$_2$ crystal.
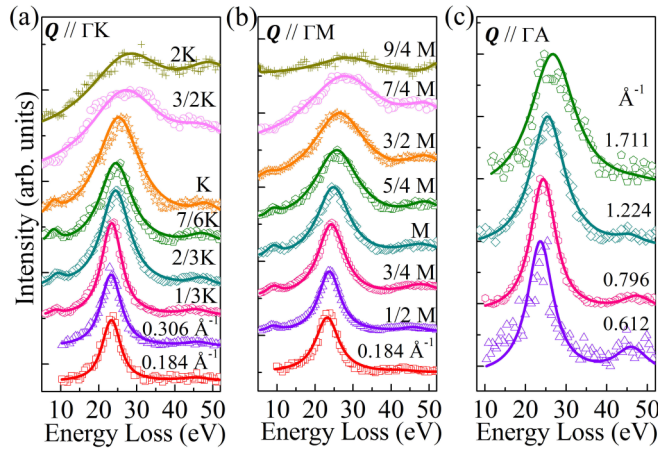
FIG. 2. IXS spectra of the MoS_2 single crystal. (a) Q along $\Gamma\underline{K}$; (b) Q along $\Gamma\underline{M}$; and (c) Q along $\Gamma\underline{A}$. All spectra have been normalized by the incident-beam intensity. Solid curves are the fitting functions.

For the $Q // \Gamma M$ direction, we also collected eight spectra shown in Fig. 2(b) from $Q = 0.184$ to $Q = 2.65$ Å^{-1} (9/4 ΓM in the Brillouin zone). Note that we could not measure it at lower momentum values because of the increasing contribution of the elastic peak for $Q \to 0$ (Γ point). The signal became stronger with increasing momentum and the spectra intensity reached a maximum when $Q = 0.883$ Å^{-1} (2/3 K) and $Q = 0.861$ Å^{-1} (3/4 M) for the ΓK and ΓM directions, respectively. After that, the intensity decreased with increasing of Q. Only four spectra are shown in Fig. 2(c) for Q along the ΓA direction due to the weak signal at both lower and higher Q. The spectra we obtained agree well with the previous EELS and optic measurements [37–41]. It should be mentioned that none of these works have investigated the plasmon dispersion behavior. A common feature of all our experimental loss function spectra is the very prominent peak near 23 eV which is associated with a plasmon excitation of the complete valence-electron gas in MoS_2. In the energy window between 2 and 52 eV, another two features can be identified at about 8.6 and 45 eV. The intermediate energy peak at around 8.6 eV, right after the elastic peak for the ΓK and ΓM direction, is supposed to arise from the oscillations of the electrons which are not involved in the ionic-covalent bonds between molybdenum and sulfur [39]. The broad peak between 40 and 50 eV represents the excitations of the $4p_{1/2}$ and $4p_{3/2}$ states of molybdenum [39]. For all three directions, the 23 eV plasmon peaks exhibit a positive dispersion with their positions' shift to higher energies as the momentum transfer increases. Clear peak broadening can also be seen with the increase of momentum.

B. MoS$_2$ plasmon dispersion

Figure 3(a) shows the peak positions of the main plasmon as a function of momentum, as determined by the fitting procedure. This plasmon displays an isotropic dispersion behavior in all three directions. When momentum is smaller than 1.1 Å^{-1}, the peak position is relatively stable and shows a slight increase with momentum. When momentum is larger
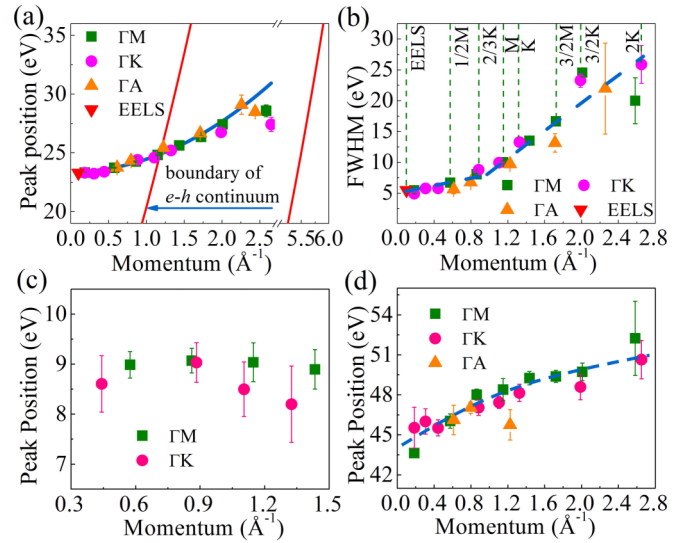

FIG. 3. The plasmon dispersion behavior. (a) Dispersion of the energy-loss peak positions for ~23 eV plasmon; (b) the ~23 eV plasmon linewidth as a function of the momentum transfer. In (a) the boundaries of the e-h continuum determined within a free-electron-gas model are indicated by dotted lines. The blue solid curve in (a) shows the parabolic fitting of the plasmon dispersion. The peak positions and FWHM were obtained by applying Voigt fits to the data, as shown in Fig. 2. The EELS data were obtained from the experiment of Habenicht *et al.* [46]. (c) The intermediate excitation near 8.6 eV and (d) the high-energy peak near 45 eV. The dashed lines in (b,d) are guides for the eyes.

than 1.1 Å^{-1}, this peak starts to shift dramatically with an increase in momentum. We also determined the plasmon linewidth FWHM from the Lorentzian contribution and its momentum dependence is shown in Fig. 3(b). This confirms its tendency to demonstrate an inflection point around the same momentum, beyond which the width of the plasmon peak increases much faster.

It is instructive to compare the measured plasmon properties with predictions of the classical free-electron-gas model where the only parameter is the average valence-electron density of the system. To make such comparison, in Fig. 3(a) we show by the dotted lines the boundaries of the electron-hole (e-h) continuum, which are determined by using the following equations based on the free-electron-gas model [42]:

$$\hbar\omega = \frac{\hbar^2}{2m}[(\mathbf{k} \pm \mathbf{Q})^2 - \mathbf{k}^2], \quad |\mathbf{k}| < k_F, \ |\mathbf{k} + \mathbf{Q}| > k_F, \quad (3)$$

where $k_F = \sqrt[3]{3\pi^2 n}$ is the Fermi wave vector, $\mathbf{k}$ is the wave vector of an electron, m is the electron mass, and n is the average valence-electron density of MoS_2. The value of k_F used here was determined as 2.156 Å^{-1}.

According to the free-electron-gas model [43], the plasmon energy $\hbar\omega_p$ is determined by

$$\hbar\omega_p = \sqrt{\frac{4\pi e^2 \hbar^2 n}{m}}. \quad (4)$$

From Eq. (4), with an assumption of $m = 1$, we obtained $\hbar\omega_p = 21.6$ eV which is quite close to our experimental

results. The difference between the plasmon energy given by the free-electron-gas model and experimental data is due to the polarizability caused by the electronic interband transitions [38]. The plasmon cutoff wave vector in the free-electron-gas model (Q_c^{FEG}) was then calculated as $Q_c^{\text{FEG}} = 1.1$ Å^{-1}; above which a plasmon effectively decays into *e-h* pairs. This result is very close to our experimental findings because as seen in Fig. 3(b) the experimental plasmon linewidth starts to increases greatly around $Q \sim 1.1$ Å^{-1} as well.

The plasmon dispersion relation for a three-dimensional (3D) system at small Qs shows a typical parabolic dispersive behavior, which is usually described by the following equation [44,45]:

$$\hbar\omega_p(Q) = \hbar\omega_p(0) + \alpha\frac{\hbar^2}{m}Q^2, \tag{5}$$

where $\hbar\omega_p(Q)$ is the Q-dependent plasmon energy, and α is the dispersion coefficient. The main plasmon dispersion measured in the experiment can be fitted well by this equation [the blue curve in Fig. 3(a)] with the dispersion coefficient of 0.14. The $\hbar\omega_p(0)$ energy of this plasmon can also be derived by fitting the experimental data and it was determined as 23.3 eV. This value agrees well with the previous EELS result shown in Fig. 3(a) (red inverted triangle) [46].

We calculated the Fermi energy of the electron gas with n corresponding to MoS$_2$ as 17.71 eV via the equation $E_F = \hbar^2 k_F^2/2m$, which is much lower than the plasmon energy of 23.3 eV. Therefore, the observed 3D isotropic dispersion of this plasmon indicates that the high-energy collective excitation in MoS$_2$ is much less influenced by the valence-band electronic structure, which is pertinent to the quasi-2D nature of its geometric structure due to these different energy scales. This measured isotropic plasmon dispersion behavior is quite different from the anisotropic behavior which has been reported in other layered materials like graphite [26] and *h*-BN [47]. In graphite, the excitations along the ΓA direction show a much smaller dispersion compared with the in-plane transitions [26]. In *h*-BN, the high anisotropy can be reflected in the differences between the spectra in plane and out of plane, while the spectra features along the ΓA direction do not exhibit any obvious dispersion as in the case of graphite [47]. On the contrary, the similarity among the dispersions along the ΓA, ΓM, and ΓK directions has been reported on a Bi$_2$Se$_3$ single crystal, with the $\pi + \sigma$ plasmon displaying the typical parabolic dispersion with Q^2 dependence in the first Brillouin zone [48].

As mentioned above, the intermediate excitation near 8.6 eV stems from the partial plasma resonant oscillations of the electrons that are not involved in the ionic-covalent bonds between molybdenum and sulfur (only six electrons per molecular), which then forms a subgroup of valence-conduction band states. This plasmon occurs when the interband transitions have been exhausted and the plasmon energy shifts to a lower energy range compared with the theoretical value of 12.5 eV, due to the polarizability of the interband transition [38]. A similar plasmon mode was also observed in MoSe$_2$ and MoTe$_2$ [39] and showed a weak momentum dependence below $Q = 0.9$ Å^{-1}, presenting isotropic dispersion behavior along the ΓK and ΓM directions, as demonstrated in Fig. 3(c). Above $Q = 0.9$ Å^{-1}, it is tantalizing to say that a softening

behavior is presented along both directions. However, considering the error bar of energy becoming larger when Q increases, the data could also be consistent with those at lower momentum and are dispersionless. Interestingly, it is hard to observe this plasmon mode along the *c* direction, which is consistent with a previous study without momentum resolution [38] indicating a strong anisotropic behavior due to its layered structure. This 8 eV mode is not a typical 2D plasmon of the electron gas but more like a very anisotropic bulk plasmon mode which does not propagate perpendicular to the layers, but is confined in the plane.

The transitions from the Mo core electron on the *p* state to the not fully filled *d* state can produce a peak at an energy of 40–50 eV. The intensity of this core level transition is much lower than the intensity of the plasmon induced by the valence-conductance band transition. A previous energy-loss spectra study of MoS$_2$ gives a core transition with peak energy at 42.7 eV [39] while our IXS experiment gives a feature near 44 eV at the smallest momentum we investigated [shown in Fig. 3(d)]. Contrary to the intermediate plasmon mode, this core level transition shows a clear positive energy shift when momentum increases.

C. Theoretical calculations

To further study the dispersion behavior of the plasmons near 8.6 and 23 eV, we carried out *ab initio* theoretical calculations based on the time-dependent density-functional theory [29,30]. We obtained the energy-loss function Im[$\varepsilon^{-1}(Q,\omega)$] spectra, which are proportional to the inelastic scattering cross section measured by the inelastic x-ray scattering spectroscopy in the first-order Born approximation [49] as presented in Fig. 4. For the main plasmon near 23 eV, the dispersion behavior along the ΓK, ΓM, and ΓA symmetry directions in Figs. 4(a)–4(c), respectively, is almost identical, especially at small Qs. The plasmon intensity is a little higher along the ΓA direction when Q is 0.5 Å^{-1} less than along the ΓK and ΓM directions. The plasmon damping increases quickly when Q exceeds a value of 1.2−1.3 Å^{-1}, which is just close to the critical momentum transfer Q_c^{FEG} ($\sim$1.1 Å^{-1}), due to a more efficient decay into the *e-h* pairs. Above $Q \approx 2.4$ Å^{-1}, the plasmon signal becomes indiscernible in accord with the experimental results. The averaged calculated plasmon dispersion can be fitted in a wide momentum range by Eq. (5) with $\hbar\omega_p(0) = 23.0$ eV and $\alpha = 0.29$. It is shown by white dashed lines in Figs. 4(a)–4(c). It is interesting to contrast these values with predictions of the free-electron-gas model [50,51] which gives $\hbar\omega_p(0) = 21.6$ eV and $\alpha = 0.49$. In the same figures the diamonds demonstrate the fitted experimental plasmon dispersion. One can observe that at momentum smaller than $Q \approx 1$ Å^{-1} the experimental curve is rather close to the calculated plasmon peak position. However, since the coefficient α obtained in the experiment is significantly smaller than that obtained in the *ab initio* calculations the experimental plasmon dispersion curve starts to deviate notably from the calculated plasmon peak position when Q exceeds this value. It signals that the exchange-correlation effects beyond the TD-LDA may play some role in the determination of the plasmon dispersion in MoS$_2$.
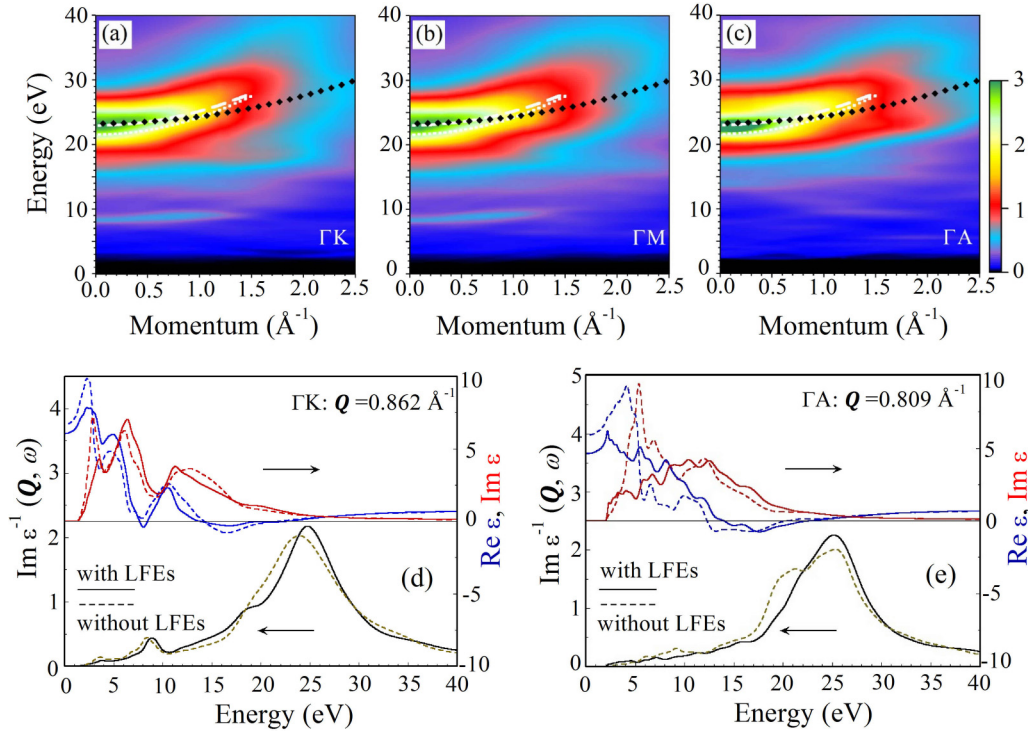
FIG. 4. Theoretical calculation results. Calculated loss function, Im[$\varepsilon^{-1}(\boldsymbol{Q},\omega)$], of MoS_2 with plasmon modes near 8.6 and 23 eV by employing a time-dependent local-density approximation (TD-LDA) for description of the dynamical exchange-correlation effects. (a–c): ΓK, ΓM, and ΓA symmetry directions, respectively. The diamonds present the fitted experimental plasmon dispersion. Dashed white lines show the fitted plasmon dispersion described by Eq. (5) with $\hbar\omega_p(0) = 23.0$ eV and $\alpha = 0.29$. Dotted white lines demonstrate the dispersion predicted by the free-electron-gas model with parameters $\hbar\omega_p(0) = 21.6$ eV and $\alpha = 0.49$. (d,e) the energy-loss spectra and dielectric function $\varepsilon(\boldsymbol{Q},\omega)$ calculated at certain momentum with/without inclusion of the local field effects at ΓK and ΓA directions, respectively.

The plasmon near 8.6 eV exists only along the ΓK and ΓM symmetry directions and is absent along the ΓA direction. At the low-momentum-transfer region below 0.9 Å^{-1}, the dispersion behavior of this low-energy plasmon is identical. Some minor differences present along the ΓK and ΓM directions when $\boldsymbol{Q}$ is higher than 0.9 Å^{-1}: The dispersion behavior follows a slightly negative trend along ΓK while it continues to follow a positive trend along ΓM. These characteristics are almost consistent with the experimental data, though the experimental data show a bigger uncertainty at higher momentum due to the weak intensity and low fitting merit.

We also conducted a RPA calculation of the excitation spectra in MoS_2 (presented in Figs. S4–S6 in the Supplemental Material [36]). Without consideration of the exchange-correlation effects at the TD-LDA level, the intensity of the plasmon peak near 23 eV declines by ∼10% for $\boldsymbol{Q} <∼ 0.5$ Å^{-1} and the peak broadens by a value of ∼0.3 eV (FWHM). In addition, careful comparison of the 23 eV plasmon peak position shows that the RPA calculation overestimates the plasmon energy in comparison with the TD-LDA at small momenta by about 0.3 eV. This difference increases up to ∼1 eV at large $\boldsymbol{Q}$s. These results suggest that exchange-correlation effects play an important role in the collective electronic excitations in MoS_2. The local field effects (LFEs) are also examined using the TD-LDA. As presented in Figs. 4(d) and 4(e), there are notable changes in the dielectric function in the low-energy

region along both the ΓK and ΓA directions (ΓM is similar to the case of ΓK, and is shown in Fig. S7 [36]), and the energy-loss peaks shift slightly upward when the LFEs are included. One can notice in these data a weak peak near 20 eV, but we did not consider it in our experimental data fitting process due to its relatively weak contribution. In Fig. 4(e), the ∼20 eV peak is pronounced when the LFEs are not included in the calculation and makes a significant contribution to the energy-loss spectrum, which is not consistent with experimental data. Hence, the LFEs are also an important factor for determination of the plasmon properties and cannot be ignored.

Considering that the truly 2D (one or more monolayers) MoS_2 systems are more relevant to device applications, we also tried to predicate their dielectric response here. When the material dimension reduces from 3D bulk to 2D monolayer, the ∼23 eV plasmon may exhibit a behavior like the ∼8.6 eV plasmon and would only show in-plane dispersion and the energy-loss positions would also shift. The behavior might be similar to that observed in graphene [24,52]. One recent work on few-layer MoS_2 using EELS and time-dependent density-functional theory (TD-DFT) calculations shows that the energy-loss position of the bulk plasmon shifts to 19.7–20.7 eV, while the lower-energy plasmon shifts to 8.3 eV [53]. However, their plasmon dispersion behaviors have not been provided by experiment results. To get the real response of

a monolayer, further experiments and calculations are still needed.

V. CONCLUSIONS

We studied high-energy collective electron excitation in a 2D structured MoS_2 single crystal via inelastic x-ray scattering. A strong plasmon mode was found near 23 eV and two weak modes appear near 9 and 45 eV. The main plasmon near 23 eV showed an unexpected 3D isotropic dispersion behavior and was very consistent with our theoretical calculations. The exchange-correlation effects and local field effects were investigated and proved significant; both must be included for accurate calculations of the plasmons in MoS_2. This work provides clear experimental and theoretical data on the dynamic electronic behavior of excited high-energy electrons,

which is beneficial for electronic device designs based on MoS_2.

[1] A. H. Castro Neto, F. Guinea, N. M. R. Peres, K. S. Novoselov, and A. K. Geim, Rev. Mod. Phys. **81**, 109 (2009).

[2] T. Ando, A. B. Fowler, and F. Stern, Rev. Mod. Phys. **54**, 437 (1982).

[3] H. S. S. Ramakrishna Matte, A. Gomathi, A. K. Manna, D. J. Late, R. Datta, S. K. Pati, and C. N. R. Rao, Angew. Chem. **122**, 4153 (2010).

[4] T. J. Constant, S. M. Hornett, D. E. Chang, and E. Hendry, Nat. Phys. **12**, 124 (2016).

[5] L. J. Wong, I. Kaminer, O. Ilic, J. D. Joannopoulos, and M. Soljačić, Nat. Photonics **10**, 46 (2016).

[6] R. Raccichini, A. Varzi, S. Passerini, and B. Scrosati, Nat. Mater. **14**, 271 (2015).

[7] S. Lee, A. Reuveny, J. Reeder, S. Lee, H. Jin, Q. Liu, T. Yokota, T. Sekitani, T. Isoyama, Y. Abe, Z. Suo, and T. Someya, Nat. Nanotechnol. **11**, 472 (2016).

[8] B. Arnaud, S. Lebègue, P. Rabiller, and M. Alouani, Phys. Rev. Lett. **96**, 026402 (2006).

[9] Y. Kubota, K. Watanabe, O. Tsuda, and T. Taniguchi, Science **317**, 932 (2007).

[10] G. Cassabois, P. Valvin, and B. Gil, Nat. Photonics **10**, 262 (2016).

[11] E. J. Sie, J. W. McIver, Y.-H. Lee, L. Fu, J. Kong, and N. Gedik, Nat. Mater. **14**, 290 (2015).

[12] K. F. Mak, K. L. McGill, J. Park, and P. L. McEuen, Science **344**, 1489 (2014).

[13] X. Yin, Z. Ye, D. A. Chenet, Y. Ye, K. O'Brien, J. C. Hone, and X. Zhang, Science **344**, 488 (2014).

[14] W. Wu, L. Wang, Y. Li, F. Zhang, L. Lin, S. Niu, D. Chenet, X. Zhang, Y. Hao, T. F. Heinz, J. Hone, and Z. L. Wang, Nature **514**, 470 (2014).

[15] X. Xi, L. Zhao, Z. Wang, H. Berger, L. Forró, J. Shan, and K. F. Mak, Nat. Nanotechnol. **10**, 765 (2015).

[16] C.-H. Du, W. J. Lin, Y. Su, B. K. Tanner, P. D. Hatton, D. Casa, B. Keimer, J. P. Hill, C. S. Oglesby, and H. Hohl, J. Phys.: Condens. Matter **12**, 5361 (2000).

[17] A. Kuc, N. Zibouche, and T. Heine, Phys. Rev. B **83**, 245213 (2011).

[18] Y. Zhang, T.-R. Chang, B. Zhou, Y.-T. Cui, H. Yan, Z. Liu, F. Schmitt, J. Lee, R. Moore, Y. Chen, H. Lin, H.-T. Jeng, S.-K. Mo, Z. Hussain, A. Bansil, and Z.-X. Shen, Nat. Nanotechnol. **9**, 111 (2014).

[19] K. F. Mak, C. Lee, J. Hone, J. Shan, and T. F. Heinz, Phys. Rev. Lett. **105**, 136805 (2010).

[20] J. K. Ellis, M. J. Lucero, and G. E. Scuseria, Appl. Phys. Lett. **99**, 261908 (2011).

[21] Z. Yin, H. Li, H. Li, L. Jiang, Y. Shi, Y. Sun, G. Lu, Q. Zhang, X. Chen, and H. Zhang, ACS Nano **6**, 74 (2012).

[22] B. Radisavljevic, A. Radenovic, J. Brivio, V. Giacometti, and A. Kis, Nat. Nanotechnol. **6**, 147 (2011).

[23] D. Sarkar, X. Xie, W. Liu, W. Cao, J. Kang, Y. Gong, S. Kraemer, P. M. Ajayan, and K. Banerjee, Nature **526**, 91 (2015).

[24] M. Pisarra, A. Sindona, M. Gravina, V. M. Silkin, and J. M. Pitarke, Phys. Rev. B **93**, 035440 (2016).

[25] Y. Lin, X. Ling, L. Yu, S. Huang, A. L. Hsu, Y.-H. Lee, J. Kong, M. S. Dresselhaus, and T. Palacios, Nano Lett. **14**, 5569 (2014).

[26] N. Hiraoka, H. Ishii, I. Jarrige, and Y. Q. Cai, Phys. Rev. B **72**, 075103 (2005).

[27] P. Cudazzo, K. O. Ruotsalainen, C. J. Sahle, A. Al-Zein, H. Berger, E. Navarro-Moratalla, S. Huotari, M. Gatti, and A. Rubio, Phys. Rev. B **90**, 125125 (2014).

[28] D. Pines and P. Nozières, *The Theory of Quantum Liquids: Normal Fermi Liquids* (W. A. Benjamin, New York, 1966), Vol. 1.

[29] E. Runge and E. K. U. Gross, Phys. Rev. Lett. **52**, 997 (1984).

[30] M. Petersilka, U. J. Gossmann, and E. K. U. Gross, Phys. Rev. Lett. **76**, 1212 (1996).

[31] V. M. Silkin, E. V. Chulkov, and P. M. Echenique, Phys. Rev. B **68**, 205106 (2003).

[32] V. M. Silkin, E. V. Chulkov, I. Y. Sklyadneva, and V. E. Panin, Sov. Phys. J. **27**, 762 (1984).

[33] D. M. Ceperley and B. J. Alder, Phys. Rev. Lett. **45**, 566 (1980).

[34] N. Troullier and J. L. Martins, Phys. Rev. B **43**, 1993 (1991).

[35] E. Gross, J. Dobson, and M. Petersilka, *Density Functional Theory II* (Springer, Berlin, 1996), p. 81.

[36] See Supplemental Material at http://link.aps.org/supplemental/10.1103/PhysRevB.96.125118 for data processing details and more calculation results.

[37] W. Y. Liang and S. L. Cundy, Philos. Mag. **19**, 1031 (1969).

[38] K. Zeppenfeld, Opt. Commun. **1**, 377 (1970).

[39] M. G. Bell and W. Y. Liang, Adv. Phys. **25**, 53 (1976).

[40] J. Bandet, A. Malavaud, and Y. Quemener, J. Phys. C: Solid State Phys. **13**, 5657 (1980).

[41] L. Martin, R. Mamy, A. Couget, and C. Raisin, Phys. Status Solidi B **58**, 623 (1973).

[42] K. Kimura, K. Matsuda, N. Hiraoka, T. Fukumaru, Y. Kajihara, M. Inui, and M. Yao, Phys. Rev. B **89**, 014206 (2014).

[43] D. Pines, *Elementary Excitations in Solids* (Perseus, New York, 1966).

[44] H. Raether, *Excitation of Plasmons and Interband Transitions by Electrons* (Springer, Berlin, 1980).

[45] R. F. Egerton, *Electron Energy-Loss Spectroscopy in the Electron Microscope* (Springer Science & Business Media, Berlin, 2011).

[46] C. Habenicht, M. Knupfer, and B. Büchner, Phys. Rev. B **91**, 245203 (2015).

[47] S. Galambosi, L. Wirtz, J. A. Soininen, J. Serrano, A. Marini, K. Watanabe, T. Taniguchi, S. Huotari, A. Rubio, and K. Hämäläinen, Phys. Rev. B **83**, 081413 (2011).

[48] S. C. Liou, M. W. Chu, R. Sankar, F. T. Huang, G. J. Shu, F. C. Chou, and C. H. Chen, Phys. Rev. B **87**, 085126 (2013).

[49] X. Zubizarreta, V. M. Silkin, and E. V. Chulkov, Phys. Rev. B **90**, 165121 (2014).

[50] C. A. Ullrich, *Time-Dependent Density-Functional Theory: Concepts and Applications* (Oxford University Press, Oxford, 2011).

[51] G. Giuliani and G. Vignale, *Quantum Theory of the Electron Liquid* (Cambridge University Press, Cambridge, 2005).

[52] P. Wachsmuth, R. Hambach, M. K. Kinyanjui, M. Guzzo, G. Benner, and U. Kaiser, Phys. Rev. B **88**, 075433 (2013).

[53] H. C. Nerl, K. T. Winther, F. S. Hage, K. S. Thygesen, L. Houben, C. Backes, J. N. Coleman, Q. M. Ramasse, and V. Nicolosi, npj 2D Mater. Appl. **1**, 2 (2017).